AIAA JOURNAL
Vol. 39, No. 12, December 2001

Modeling of Controlled Shock-Wave/Boundary-Layer Interactions in Transonic Channel Flow

Richard Benay,* Pascal Berthouze,† and Reynald Bur‡
ONERA, 92190 Meudon, France

The importance of systems aimed at controlling shock-wave/boundary-layer interactions appears for transport aircraft in the domain of transonic external flows and for supersonic air intakes in the domain of internal flows. The calibration of these systems requires powerful predictive calculation methods and therefore improvements in the modeling of complex turbulent interactions. The need for validation of numerical methods and turbulence models for this field of applications has motivated experiments aimed at producing exhaustive sets of experimental data on two-dimensional configurations. These kinds of experimental cases are very useful for model testing because they permit numerous parametrical numerical studies. This program has been completed in its experimental and theoretical part for the case of a passive control device, which consists of a feedback of the external flow through a cavity, covered by a perforated plate located in interaction region. The main results are presented, and the legitimacy of modeling injection by Poll's law is confirmed. The recently defined k–σ turbulence model is validated, and its results are compared with those given by the Chien and Launder–Sharma versions of the k–ε model. The new model, primarily tested in the case of supersonic backward-facing step separations, has given satisfactory results too in simulating these transonic internal flows.

Nomenclature

C_μ	=	constant for eddy viscosity
d	=	hole diameter of the perforated plate
$e, \tilde{e}, e^*$	=	energy per unit mass; instantaneous, Favre averaged, generalized
$i, \tilde{i}, i^*$	=	internal energy; instantaneous, Favre averaged, generalized
K	=	porous wall coefficient
k	=	turbulent kinetic energy
M	=	Mach number
P	=	porosity of the perforated plate
P_k	=	production term
Pr, Pr_T	=	laminar and turbulent Prandtl numbers
p, p^*	=	mean and generalized static pressures
p_{st0}	=	stagnation (reservoir) pressure
Q	=	suction mass flow rate
q_j^*, q_j^{*T}	=	laminar and turbulent heat fluxes
r	=	constant of perfect gases
T	=	static temperature
T_{ij}	=	total tensor of molecular constraints
T_{st0}	=	stagnation temperature
t	=	time, thickness of the perforated plate
$\tilde{U}_i$	=	mean velocity components
U_0	=	reference velocity, 384 m/s
u_i''	=	theoretical Favre fluctuating velocity components
u, v	=	X-wise and Y-wise mean velocity components
u', v'	=	X-wise and Y-wise velocity fluctuations
$-\overline{u'v'}$	=	cross correlation of velocity fluctuations
X	=	streamwise coordinate along the channel lower wall, origin at the nozzle throat
x_i	=	Cartesian coordinates
Y	=	coordinate normal to the channel lower wall
Y^+	=	reduced distance from the wall
β	=	constant of the k–ω model
γ	=	ratio of specific heats
Δ	=	Laplace operator
δ	=	constant of the k–σ model
δ^*	=	boundary-layer displacement thickness
ε	=	turbulent dissipation
μ, μ_T	=	laminar and eddy viscosities
ν	=	molecular kinematic viscosity coefficient
ρ	=	density
σ	=	mean free path of turbulent eddies
τ_{ij}, τ_{ij}^T	=	molecular and turbulent shear-stress tensors
χ	=	constants for diffusion terms

Introduction

THE interest in various concepts of flow control is now well established; their resulting technical applications are widely used for improving performance of aerospace vehicles. These techniques concern both external and internal aerodynamics. Particularly important phenomena that have to be controlled are the interactions between shock waves and the boundary layer occurring on the wing of transonic transport aircraft. Techniques for achieving control of this interaction can be roughly classified into two families, namely, 1) control by variations of the profile's geometry and 2) control by boundary-layer manipulation. This last family of techniques implies the addition of suction or blowing devices that can compromise performance of the overall vehicle specifically by the weight added by their presence. Boundary-layer manipulation is also used for internal flows mainly in the case of supersonic inlets to reduce or prevent separation at shock impingement location. Manipulation techniques are expected to reduce the shock strength and to bleed off the boundary layer, thus reducing separation and/or preventing flow fluctuations.

Boundary-layer manipulation tools can themselves be classified into two subfamilies: active control devices that suck a part of the boundary layer through a slot and passive control devices. It is recalled that the principle of passive control consists of establishing a natural circulation between the high-pressure region downstream of a shock and the upstream low-pressure region. This circulation is achieved through a cavity covered by a perforated plate and placed underneath the shock foot region.[1,2] Passive control vs active control presents the advantage of not including the supplementary weight and cost of an external suction device. It has been shown that, in

Received 27 January 2001; revision received 7 May 2001; accepted for publication 18 May 2001.

*Head, Database/Theoretical Exploitation, Experimental/Fundamental Aerodynamics Department, 8 Rue des Vertugadins.

†Ph.D. Student, Experimental/Fundamental Aerodynamics Department, 8 Rue des Vertugadins.

‡Research Scientist, Experimental/Fundamental Aerodynamics Department, 8 Rue des Vertugadins. Member AIAA.

very limited circumstances, passive control may produce a reduction of an airfoil drag, while postponing to higher incidences the limit of buffet onset.[3] This control, when employed in supersonic mixed compression inlets, appears to be more promising.[4,5] In these cases the suppression of large separated flow resulting from the strong interaction of the oblique shock avoids significant efficiency losses in the air intake and flow distortion at the engine entry. Unsteady phenomena caused by oscillations of the terminal normal shock are also eliminated because of its stabilization by passive control. A technique derived from the two former ones is hybrid control, which is a combination of a passive control cavity and a suction slot (or cavity) located downstream of it.

The objective of the present study was to contribute to the understanding and modeling of the physical phenomena involved in a shock-wave/boundary-layer interaction under control conditions. This work was first based on execution of basic experiments aiming at detailed descriptions of the interacting flowfield in cases of passive,[6] active, and hybrid control.[7] These experiments furnished a database for the second phase of the study, which was the improvement of the physical models implemented in methods used to predict shock-wave/boundary-layer interactions under control conditions. A major point of interest in the theoretical part of the study, whose results will be presented here, was the ability of the two-equation turbulence models to reproduce the evolution of mean and fluctuating velocity fields.

The experiments were performed in a two-dimensional transonic channel and examined the interaction between the shock crossing the channel and the boundary layer developing on the channel lower wall. The mean and turbulent properties of the interaction domain were determined by means of laser Doppler velocimetry (LDV) measurements. Numerical simulations of the channel flow have been carried out with a code solving the Reynolds-averaged Navier–Stokes (RANS) equations. RANS calculations have become a tool for obtaining finer predictions of profiles or inlet aerodynamic performance in the industry. At a fundamental level, testing more direct simulation tools such as large eddy simulation (LES) still demands, for accurate predictions of such flows, computing capabilities that will not be reached in the near future. Analytical laws were tested as boundary conditions to be prescribed at the wall in the control region. Comparisons of experimental and numerical results were made for the reference case (without control) and for a passive control case.

Basic Equations and Presentation of the Turbulence Models

In the present framework of RANS calculations, the basic transport equations for the flow, as a consequence of the use of Boussinesq's hypothesis, take the following form:

$$\frac{\partial \bar{\rho}}{\partial t} + \frac{\partial \bar{\rho}\tilde{U}_l}{\partial x_l} = 0 \tag{1}$$

$$\frac{\partial \bar{\rho}\tilde{U}_l}{\partial t} + \frac{\partial \bar{\rho}\tilde{U}_l\tilde{U}_j}{\partial x_j} = -\frac{\partial p^*}{\partial x_l} + \frac{\partial}{\partial x_j}\left(\tau_{jl} + \tau_{jl}^T\right) \tag{2}$$

$$\frac{\partial \bar{\rho}e^*}{\partial t} + \frac{\partial \bar{\rho}e^*\tilde{U}_j}{\partial x_j} = -\frac{\partial p^*\tilde{U}_j}{\partial x_j} + \frac{\partial}{\partial x_j}\left[\left(\tau_{jl} + \tau_{jl}^T\right)\tilde{U}_l\right] - \frac{\partial}{\partial x_j}\left(q_j^* + q_j^{*T}\right) + D(k) - \left[1 - \frac{2}{3(\gamma-1)}\right](P_k - \rho\varepsilon) \tag{3}$$

with

$$D(k) = \frac{2}{3(\gamma-1)}\frac{\partial}{\partial x_j}\left[\left(\mu + \frac{\mu_T}{\chi_k} - \gamma\frac{\mu}{Pr} - \gamma\frac{\mu_T}{Pr_T}\right)\frac{\partial k}{\partial x_j}\right]$$

In these equations, - designates Reynolds averaging and $\sim$ Favre averaging. The starred variables are introduced in order to take into account the turbulent kinetic energy. The various preceding terms have the following definitions:

$$p^* = p + \tfrac{2}{3}\bar{\rho}k$$

$$p^* = (\gamma-1)\bar{\rho}i^* \qquad \text{with} \qquad i^* = \tilde{i} + \frac{2}{3(\gamma-1)}k$$

$$\tilde{i} = \frac{rT}{\gamma-1}, \qquad e^* = i^* + \frac{\tilde{U}_l\tilde{U}_l}{2}$$

$$\tau_{jl} + \tau_{jl}^T = (\mu + \mu_T)\left(\frac{\partial \tilde{U}_j}{\partial x_l} + \frac{\partial \tilde{U}_l}{\partial x_j} - \frac{2}{3}\delta_{jl}\frac{\partial \tilde{U}_m}{\partial x_m}\right)$$

$$q_j^* + q_j^{*T} = -\gamma\left(\frac{\mu}{Pr} + \frac{\mu_T}{Pr_T}\right)\frac{\partial i^*}{\partial x_j}, \qquad P_k = -\overline{\rho u_k'' u_l''}\frac{\partial \tilde{U}_k}{\partial x_l}$$

is the production term and $\rho\varepsilon$ the dissipation term. This choice of variables, considering k as a component of the pressure, keeps the familiar form of the viscous gas dynamics equations with the only exception of the two last terms of the right-hand side of the energy equation. These two terms, small in comparison with the others in this equation, are source terms approximated explicitly, the others being treated implicitly.[8]

For the evaluation of the eddy viscosity used in this global formulation as a function of two fundamental turbulent scales of the flow, we will concentrate our attention on a newly introduced k–σ model[9] derived from both k–ω[10] and k–ε renormalized[11] (RNG) models. The results obtained with this model will be compared with the Chien[12] (Ch) and Launder–Sharma[13] (LS) versions of the k–ε model.

The transport equations of the turbulent kinetic energy k and its dissipation rate ε in the k–ε models are as follows.

Transport of k:

$$\frac{\partial(\rho k)}{\partial t} + \frac{\partial(\rho k\tilde{U}_i)}{\partial x_i} - \frac{\partial}{\partial x_i}\left[\left(\mu + \frac{\mu_T}{\chi_k}\right)\frac{\partial k}{\partial x_i}\right] - P_k + \rho\varepsilon + R(k) = 0 \tag{4}$$

Both models use the following well-known definition for the eddy viscosity:

$$\mu_T = C_\mu f_\mu(\rho k^2/\varepsilon) \tag{5}$$

When the k–ε model of Chien is used, we have the following:

$$\chi_k = 1, \qquad C_\mu = 0.09$$

$$R(k) = \frac{2\mu k}{(Y - Y_W)^2}, \qquad f_\mu = 1 - \exp(-0.0115Y^+)$$

with $Y^+ = (Y - Y_W)[\sqrt{(\rho_W\tau_W)}/\mu_W]$, the subscript w designating values at the wall.

In the case of the LS model:

$$\chi_k = 1, \qquad C_\mu = 0.09, \qquad R(k) = 2\mu\frac{\partial\sqrt{k}}{\partial x_i}\frac{\partial\sqrt{k}}{\partial x_i}$$

$$f_\mu = \exp\frac{-3.4}{(1 + R_T/50)^2} \qquad \text{with} \qquad R_T = \frac{\rho k^2}{\mu\varepsilon}$$

Transport of ε:

$$\frac{\partial(\rho\varepsilon)}{\partial t} + \frac{\partial(\rho\varepsilon\tilde{U}_i)}{\partial x_i} - \frac{\partial}{\partial x_i}\left[\left(\mu + \frac{\mu_T}{\chi_\varepsilon}\right)\frac{\partial\varepsilon}{\partial x_i}\right] + C_{\varepsilon 2}\rho\frac{\varepsilon^2}{k} - C_{\varepsilon 1}\frac{\varepsilon}{k}P_k + Q(\varepsilon) = 0 \tag{6}$$

For the k–ε model of Chien:

$$\chi_\varepsilon = 1.3, \qquad C_{\varepsilon 1} = 1.35, \qquad C_{\varepsilon 2} = 1.8\left[1 - \frac{2}{9}\exp\left(-\frac{R_T^2}{36}\right)\right]$$

$$Q(\varepsilon) = \frac{2\bar{\mu}f_2^*\varepsilon}{(Y - Y_W)^2}, \qquad f_2^* = \exp(-0.5Y^+), \qquad R_T = \frac{\rho k^2}{\mu\varepsilon}$$

For the LS model:

$$\chi_\varepsilon = 1.3, \qquad C_{\varepsilon 1} = 1.44, \qquad C_{\varepsilon 2} = 1.92\left[1 - 0.3\exp\left(-R_T^2\right)\right]$$

$$Q(\varepsilon) = -2(\mu\mu_T/\rho)[(\Delta u)^2 + (\Delta v)^2]$$

The k–σ turbulence model uses an evaluation of eddy viscosity as an elementary function of the local mean velocity fluctuation and a length scale σ, which has been interpreted as a "mean free path for the eddies." The eddy viscosity is then defined to be[9]

$$\mu_T = \rho\sigma\sqrt{k} \tag{7}$$

An expression of the dissipation as a function of ρ and σ is easily obtained by equating the definitions given by Eqs. (5) and (7) for μ_T in the case of fully turbulent flows ($f_\mu = 1$), the resulting value being $\varepsilon = C_\mu k^{3/2}/\sigma$. The transport equation for k in the k–σ model is Eq. (4) with $R(k) = 0$ and the use of the last evaluation for the dissipation. Models have generally to be improved near the wall by adding an intermittence factor f_μ to the eddy viscosity and various damping factors on source terms for the transport of eddy viscosity variables. General rules for establishing such damping functions are still under study. For the k–σ model we just use the following factor, which has the well-known general form

$$f_\mu = 1 - \exp(-At/\tau) \tag{8}$$

Here t/τ is the ratio of a turbulent and a laminar characteristic time[9]; explicitly, we have $t/\tau = (\mu_T/\mu)(rT/k)\cdot A$ is an empirical constant aimed at calibrating the model to improve for noninteracting boundary layers the fitting with experiment of the predicted Reynolds-stress tensor. This empirical constant is not universal because it has been noted in recent experimental studies that the influence of wall roughness on Reynolds-stress level is considerable.[14] We determined in Ref. 9 that fixing the value of A around 1/4000 gave the best improvement in the prediction of the supersonic boundary layer developing along a smooth cylindrical sting. This last value appeared to be adequate too for the present channel flow with smooth walls, where f_μ provides a fine tuning of the level of computed shear stresses in the boundary layer before interaction.

The transport equation for the mean free path σ has first been established in the case of homogeneous turbulence without wall effects. In this case this equation was deduced from that for the characteristic frequency ω established in the k–ω model of Wilcox[10] and the transport equation for k by a change of variables. This was done by equating Eq. (7) to the k–ω definition for μ_T, which is in fully turbulent flows[10]:

$$\mu_T = \rho(k/\omega) \tag{9}$$

The transport equation for σ had to be modified to take into account more general physical situations. The first essential modification was the use of the common value 0.7179 for the constant dividing μ_T in all of the turbulent diffusion terms relative to the scalar quantities transported in the flow. The effective constancy of this generalized Prandtl number is established and used in the RNG analysis.[15] It was necessary to introduce in the transport equation for σ a source term to account for large strain rate effects. By considering the RNG model, this source term has been chosen to be a linear function of the production source term for ε transport defined in this last model. (Detailed explanations and motivations for all of these choices can be found in Ref. 9.)

The resulting second transport equation of the k–σ model is then the following one:

$$\frac{\partial\rho\sigma}{\partial t} + \frac{\partial\rho\sigma\tilde{U}_j}{\partial x_j} - \frac{\partial}{\partial x_j}\left|\left(\mu + \frac{\mu_T}{0.7179}\right)\frac{\partial\sigma}{\partial x_j}\right|$$

$$= \left(\mu + \frac{\mu_T}{0.7179}\right)\left(\frac{1}{4}\frac{\sigma}{k^2}\frac{\partial k}{\partial x_j}\frac{\partial k}{\partial x_j} - \frac{2}{\sigma}\frac{\partial\sigma}{\partial x_j}\frac{\partial\sigma}{\partial x_j} + \frac{1}{k}\frac{\partial\sigma}{\partial x_j}\frac{\partial k}{\partial x_j}\right)$$

$$+ \left(\frac{1}{2} - \delta C_\varepsilon\right)\frac{\sigma}{k}P_k + \left(\frac{\beta}{C_\mu} - \frac{1}{2}\right)\rho C_\mu k^{\frac{1}{2}}$$

with $\delta = 5/9/1.42$; $C_\mu = 0.0837$; $\beta = \frac{3}{40}$; $C_\varepsilon = 1.42 - [\eta(1-\eta/4.38)/(1+0.015\eta^3)]$; η being function of the ratio of the turbulent kinetic energy production to the dissipation rate[11]: $\eta = \sqrt{(P_k/C_\mu\rho\varepsilon)}$.

Experimental Conditions and Tested Configurations

Experiments aimed at providing data for the validation of theoretical models were executed in a transonic-supersonic continuous wind tunnel supplied with desiccated atmospheric air.[6] It consists of a transonic channel having a test section with a height of 100 mm and a span of 120 mm (Fig. 1). The lower wall is rectilinear and equipped to receive the cavity for passive control (whose longitudinal cut view can be seen in Fig. 1), whereas the upper wall is a contoured profile designed to produce a uniform supersonic flow of nominal Mach number equal to 1.4. The stagnation conditions are $p_{st0} = 92{,}000 \pm 500$ Pa and $T_{st0} = 300 \pm 3$ K. A second throat of adjustable cross section is placed in the test-section outlet to produce by choking effect a shock wave whose position can be monitored in a continuous and precise manner.

The cavity for passive control is 70 mm long and 60 mm deep and occupies the entire width of the test channel (Fig. 1). The cavity is covered by a perforated plate, whose nominal characteristics are porosity $P = 5.67\%$ (the porosity is the ratio between the sum of the hole exit surfaces and the total surface of the plate), holes of diameter $d = 0.3$ mm normal to the lower wall plane, and perforated plate thickness $t = 1$ mm. This cavity begins 130 mm downstream of the first throat; the lower wall at the level of this throat in the

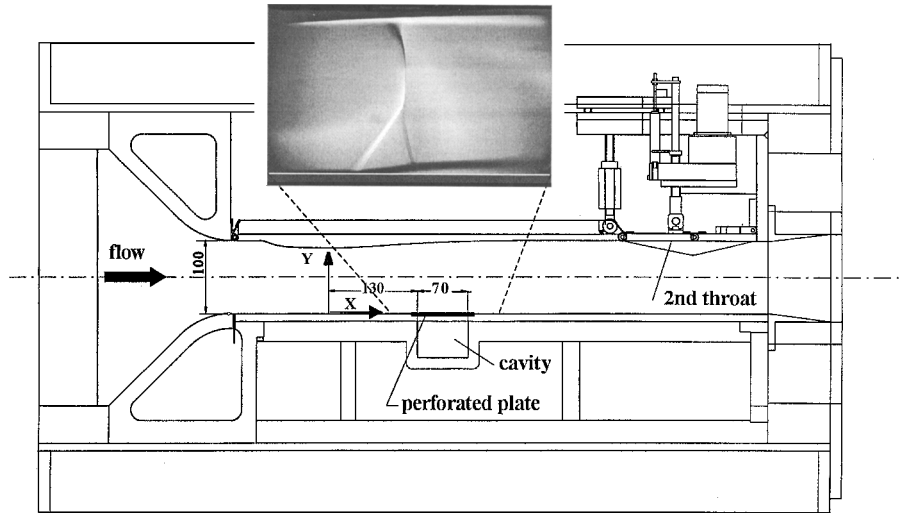

Fig. 1 Passive control experimental setup (dimensions in millimeters).

median longitudinal plane is taken to be the origin of coordinates. The location of the shock wave in the outer part of the flow is fixed at middistance between the origin and the end of the cavity, this location being accurately obtained by considering the pressure distribution on the channel upper wall. A reference case with a solid lower wall was tested in order to allow comparisons with the control configuration.

The flows under study are qualified by schlieren visualizations (a schlieren of the controlled interaction is shown in Fig. 1) and measurements of wall-pressure distributions and instantaneous velocity fields. For the present nominally two-dimensional flow (confirmed by probing in planes located at ± 20 mm from the median plane of the test section in the interaction region[16]), the latter are obtained with a two-component LDV system operated in the forward-scattering mode.[6] The flow is seeded with submicronic (0.5-μm-diam) droplets of olive oil injected in the wind-tunnel settling chamber.

The field quantities are given with an accuracy mainly depending on uncertainties affecting the LDV system calibration and the statistical treatment of the sample of the instantaneous velocity components. For the present experiments these uncertainties are 1) 1% of the maximum velocity modulus (i.e., the velocity U_0 of the upstream external flow, equal to 384 m/s and taken as reference) for the mean velocity components, 2) less than or equal to 8% of the maximum normal stress for the normal stress components of the Reynolds tensor, and 3) less than or equal to 10% of the maximum shear stress for the turbulent shear-stress component.

The flowfields have been explored along lines normal to the wall (Y direction) extending from the surface ($Y = 0$) to an altitude $Y = 22$ mm and contained in the test-section median plane. This extent is chosen to be sure to cover the entire dissipative layer and a part of the outer inviscid flow. Their streamwise locations are in the range 115 mm $\leq X \leq$ 260 mm including the control region. Reliable measurements with the LDV system, in this two-component version, are limited to a minimum distance of 0.3 mm from the wall.

Flow Modeling and Numerical Simulations

The numerical simulations were performed with the NASCA code,[8] which solves the classical RANS equations. The code, using a finite volume technique and a Beam–Warming approach in time for finding a stationary state,[17] is totally implicit, including its modules treating the turbulence transport equations. The convective fluxes, for both mean flow and turbulent quantities, are approximated basically by the Osher and Chakravarthy scheme,[18] which is total variation diminishing and precise up to third order in space following the values of its parameters. In the NASCA code this scheme has been extended to approximate the fluxes rigorously to the second order in space in meshes where important shifts occur between the size of two adjacent cells.[8] The approximations of all of the diffusive fluxes are also precise to the second order for such kinds of meshes. To test the ability of the code to accurately simulate separated flows while eliminating the uncertainties coming from the turbulence model itself, the scheme was first validated for hypersonic laminar flow.[19] The implicit mode of calculation has been extended to the transport of k and of the second fluctuating quantity. The use in Eqs. (1–3) of the generalized pressure p^*, in which the coupling variable k is absorbed, allows, in particular, to calculate successively, at a given time step, the group of mean flow variables and the two fluctuating quantities, therefore to invert (4×4) rather than (6×6) matrices at each point of the mesh.[8]

The calculation domain (Fig. 2) is a part of the experimental channel extending from a far upstream section of the divergent expanding zone (at $X = 60$ mm), where experimental velocity and turbulent shear-stress profiles are imposed to give well-defined supersonic inflow conditions, to the end of the channel, where the experimental pressure is imposed. The solution adopted here for testing turbulence models accurately consists in calculating ε or σ on the inflow boundary in such a way that experimental and modeled cross correlation of fluctuations be equal. The evaluation of k from the experiment that is necessary for this purpose necessitates the calculation of the third velocity fluctuation correlation component from the two effectively measured longitudinal ones u'^2 and v'^2. For

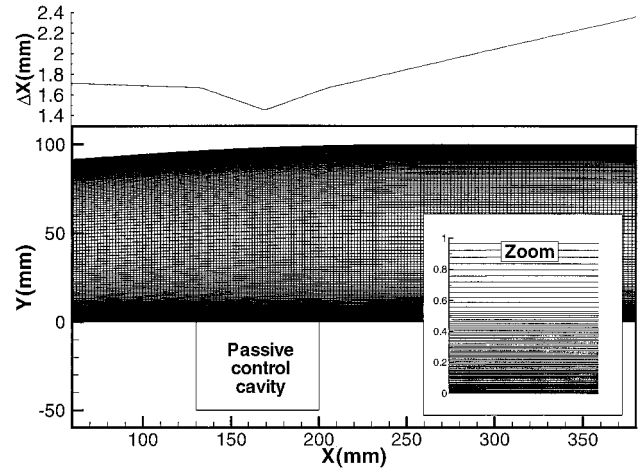

Fig. 2 Computational grid (178 × 361).

this we use the classical approximation $w'^2 \approx \frac{1}{2}(u'^2 + v'^2)$, which is questionable for the totality of the flow, and so for the validations we have focused our attention on comparisons with cross-correlation values. The second fundamental point is to impose the experiment-fitted values on the entire vertical width of the channel. The calculation domain thus includes both upper and lower walls. The tests of the turbulence models are done by comparisons with representative experimental field values obtained in a window surrounding the interaction zone of the lower wall. At the downstream boundary coinciding with the end of the channel and situated at $X = 380$ mm, a numerical procedure, which is an adaptation of the characteristic extrapolation method,[20] is developed for fixing the static pressure level.

Passive control is simulated by prescribing the unit mass flow ρv at the wall, the conditions on the other variables remaining unchanged. The ρv value at the wall is obtained by relations expressing a direct dependence of the wall vertical velocity to the pressure difference between the cavity and the external flow. The relation used for the computations is the calibration law of Poll et al.[21] To establish this law, a flow model is developed for an ideal hole. This means that the hole has a cylindrical shape and the flow in it is laminar, incompressible, and pipe like (the ratio of the plate thickness t to hole diameter d is large). For such a hole there exists a quadratic relationship between the pressure drop across the perforated surface Δp and the mass flow rate $\dot{m}$:

$$S = (1/K)(40.7Q + 1.95Q^2)$$

with

$$Q = \dot{m}/\mu t$$

$$S = (\Delta p d^2/\rho v^2)(d/t)^2$$

The preceding law is valid (ideal hole case) if

$$t/d > 0.06R_d$$

where $R_d = Vd/\nu$, V being the bulk or average velocity that is assumed constant (equal to the mean normal velocity component at the wall, or "hole velocity" v_w).

In the preceding relation one notes that a coefficient K appears. This coefficient is introduced to generalize the ideal hole case (for which $K = 1$) for practical situations. The laser-drilled sheets do not have perfect holes, the holes being larger on the side closest to the laser (plenum side) and so have an irregular conical shape. In fact, the value of K is very difficult to obtain accurately because it appears to strongly vary with the hole diameter. In this approach it is assumed that each hole behaves as if it were alone, i.e., hole-on-hole interference is likely to be small. So, the model for the entire perforated plate is based on the summation of the characteristics of a large number of independent holes.

To take these two remarks into account, one introduces the porosity P of the perforated plate. Before this let us make explicit the (Q, S) relation in terms of (v_w, p_c, p); one obtains the following parabolic relation:

$$1.21\rho v_w^2 + (32t\mu/d^2)v_w - K(p - p_c) = 0$$

In the computations the preceding equation was solved for the ideal hole case assumption, i.e., with $K = 1$. Negative solutions correspond to suction, positive solutions to injection. To obtain the velocity distribution along the perforated plate, one multiplies this hole velocity v_w by the porosity P of the perforated plate.

The cavity pressure is fixed to its measured experimental value: 56110 ± 500 Pa. The preceding wall vertical velocity law accounts for a pure dependence of the mass flow rate to the pressure difference between the cavity and the external flow. One can summarize this fact by a relation: $\rho v = f(p)$. With the streamwise velocity at the wall being constant and equal to zero, the continuity equation takes the form $\partial\rho v/\partial Y = 0$, which implies $\partial p/\partial Y = 0$. The additional hypothesis of thermal equilibrium at the wall implies the classically used relations: $\partial\rho/\partial Y = 0$, $\rho u = 0$, $\partial\rho e/\partial Y = 0$, with the simple modification $\rho v = f(p)$. The sign of the vertical velocity at the wall, positive or negative following the case of blowing or suction, is determined by the sign of the pressure difference $(p_c - p)$ between the cavity and the outer flow. The mean value of ρv being the same at both ends of the hole, the formulas can be applied at one or the other side of the perforated plate.

The (178×361) grid used (Fig. 2) has been retained after a study of space convergence of the calculation. The LS model, which is significantly more sensitive to the mesh than the two other ones, has necessitated the use of this particularly fine grid. Major attention has been paid to mesh refinement at the wall. The reduced distance Y^+, defined after Eqs. (4) and (5), is equal to 0.57 for the upstream cell close to the wall. The X distribution of the cell length in the X direction is shown at the top of Fig. 2. The search for an optimal grid has consisted in successive calculations with various refinements until the occurrence of space convergence in the viscous zones. The two more sensitive zones are the shock impingement and the near-wall flow. The best way for illustrating our final test for space convergence is to show the coincidence between results obtained with (178×381) and (355×361) grids. The differences lie in the adjunction of 10 intermediate points between the ones closer to the wall in the boundary layer and a global doubling of the points in the main flow direction (X). The skin-friction coefficient was not measured but has been chosen as an example because it is the more sensitive to variations of the mesh size (Fig. 3). It appears first that the shock position does not change by doubling the mesh longitudinally, no more than the stiffness of the gradients at its impingement. The plotted skin-friction levels are also invariant by adding points in the boundary layer. None of the other variable's longitudinal or transverse profiles in the viscous zones varies more than that shown in Fig. 3; their area of maximal relative variation is smaller than 1%. The results given here are relative to the reference case, without control of the interaction. The quality of this mesh has been verified, with the same results, in the case of a controlled interaction with the single LS model. A last remark is that the test for space convergence has been performed by looking to the viscous zones of the flow, in which the gradients caused by the shock spread rapidly. A search for a good resolution of the shock in the nonviscous zones, imposing considerable grid refinements and costly calculations, was beyond the scope of this study.

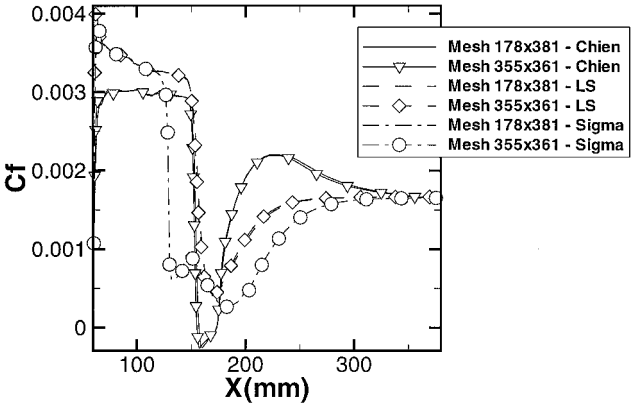

Fig. 3 Skin-friction coefficient evolution on the lower wall: reference case.

Comparisons with Experiment

Reference Case

The normalized wall-pressure distributions for the reference case are plotted in Fig. 4; the smaller than 1% error bar on the experimental values is well represented by the width of the graphical symbol used to mark them. The dip in calculated surface-pressure distribution, which is visible close to the upstream boundary situated at $X = 60$ mm, is because of the fact that the experimental field variables at this boundary were measured not closer than 0.1 mm to the wall. The upstream boundary profile values situated between 0 and 0.1 mm had to be determined by linear interpolation. The repercussion of this discrepancy on the calculated profile immediately downstream of the boundary is thus visible on Fig. 4, where the zone of "reconstruction" of a correct near-wall evolution of the fields is evidenced. The location where the shock takes place is determined by the pressure levels in the subsonic downstream flow. These pressure levels are themselves function of the effective walls formed by the boundary-layer displacement thickness that delimit the equivalent perfect fluid flow. The longitudinal evolution of this thickness depends on the models. We see therefore that they will influence strongly the location of the interaction zone. A correct prediction of this location was obtained only with the k–σ model. In the case of the k–ε calculations, it was predicted more than 20 mm upstream. Comparisons in the zone of interaction between the two types of models give, in these conditions, very large errors in the case of the k–ε. This does not give significant information on their true global quality. So, we have preferred to force a downstream pressure level lower than the measured one to adjust the shock position calculated by the k–ε models at the right place. The consequence of this choice, for a given model, is only a downstream translation of the wall-pressure step of Fig. 4 without other modification. With the velocity profiles upstream of interaction being practically invariant, the fields in the interacting viscous zones stay the same too. The price of this adjustment of the shock is that the k–ε models are submitted to a pressure step lower than the experimental one between $X = 170$ and 280 mm. This observation must be kept in mind for the following comparison of results in the downstream part of the interaction.

The evolution of the longitudinal velocity profiles is shown in Fig. 5. We recall from the preceding section that the first boundary-layer profile on the lower wall, at $X = 140$ mm downstream of the throat, is in fact the result of a calculation of the noninteracting channel flow on the entire width of the channel, because a given experimental profile was employed at $X = 60$ mm. This result proves that the models tested are well calibrated for the calculation

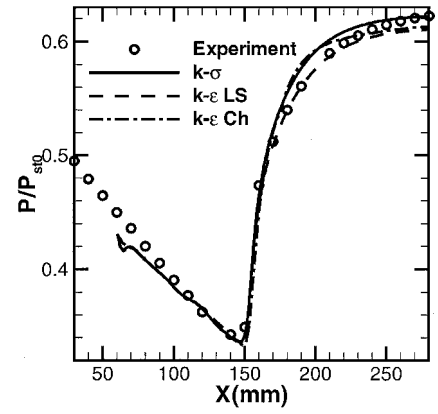

Fig. 4 Surface-pressure distribution on the lower wall: reference case.

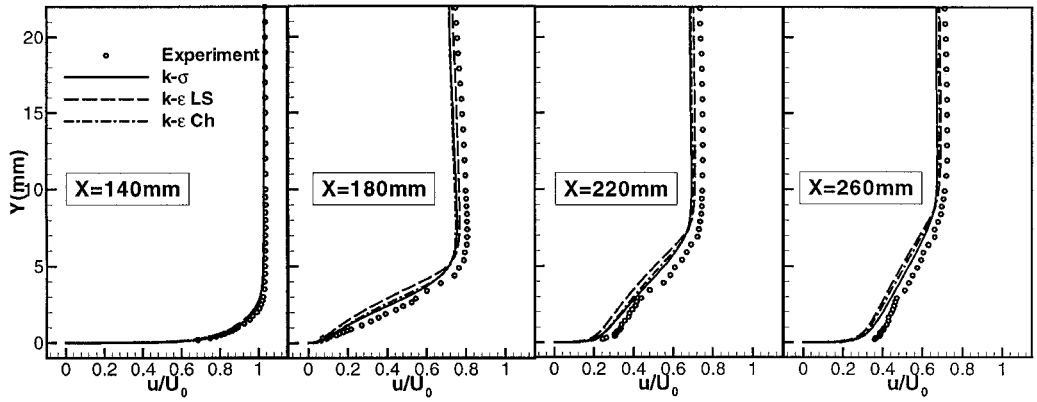

Fig. 5 Longitudinal velocity profiles: reference case.

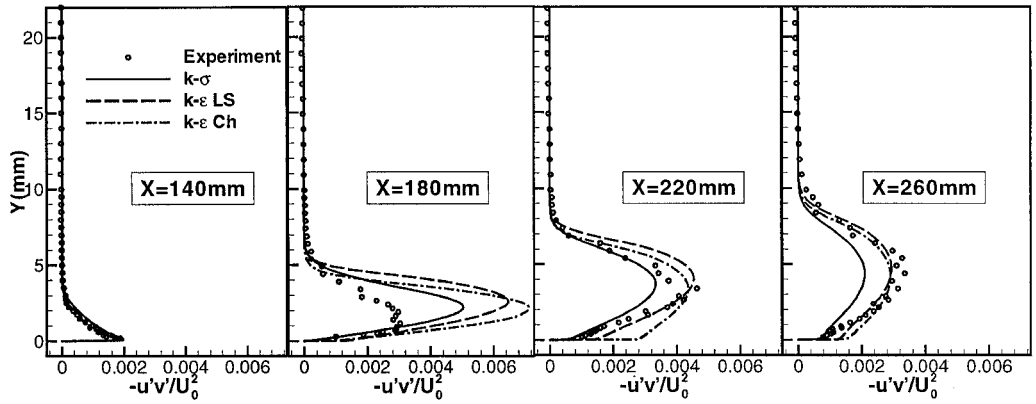

Fig. 6 Turbulent shear-stress profiles: reference case.

of two-dimensional channel flows without interaction. The second profile is situated in the interaction region at $X = 180$ mm. The agreement of the three models with experiment is satisfactory. The k–σ and LS models predict no negative longitudinal velocity components in the interacting boundary layer; the Ch model predicts a zone of such velocities of very small extension between $X = 157$ and 172 mm, extending vertically up to $Y = 0.05$ mm. Such a zone of reversed flow, if it exists, is not reachable by our measurement facilities. After the end of the interaction zone, at $X = 220$ mm the same observations can be done for the agreement of longitudinal velocities with experiment. At $X = 260$ mm, far downstream of the interaction, the boundary layer has reached a new stable state. An underestimation, whose amplitude attains 8% of U_0 in the k–ε calculations, affects the computed profiles in the boundary layer.

The computed shear stresses (calculated in Favre means: $\overline{\rho u'' v''}/\bar{\rho}$) are compared to the measured Reynolds tensor components $\overline{u'v'}$. It has been established in Ref. 22 that the difference between these two quantities is small for an adiabatic, flat-plate boundary layer, when the Mach number varies from 0 to 5. In the transonic cases the local relative discrepancy is not greater than 2%. The same observation as for mean velocities can be done about the good calibration of the models before interaction (at $X = 140$ mm; Fig. 6). In the interaction region ($X = 180$ mm) the effect of the strong pressure gradient on maximum cross-correlation level is amplified by the models with respect to experiment. The k–ε models give larger prediction of the maximum of cross-correlation levels, which will be confirmed in the downstream profiles. The prediction of the near-wall and external $\overline{u'v'}$ evolutions by all models is good. Downstream of the interaction region ($X = 220$ mm), the models fit grossly experimental evolutions, except for the near-wall behavior of the Ch model. The shift observed between the levels predicted by k–ε models on one hand and by the k–σ model on the other, at $X = 260$ mm, could be partly explained by the modification of the downstream pressure level, which implies that the profiles for the k–ε models have been submitted to lower decelerations.

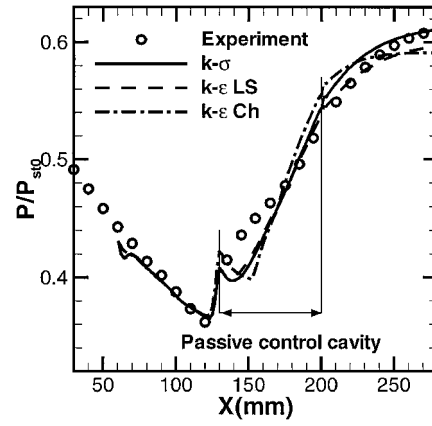

Fig. 7 Surface-pressure distribution on the lower wall with passive control.

Case with Passive Control

Computed wall-pressure distributions (Fig. 7) show the difficulty of simulating injection through very small holes with a continuous approximation made on a discrete mesh. An entirely rigorous calculation of this problem should have been done by meshing each hole, which is unrealistic with present computing capabilities. We will see in the following results that the apparently rough approximation made to treat this porous wall condition is almost correct. At the beginning of the perforated plate (Fig. 7), the peak appearing on the computed wall-pressure values at $X = 130$ mm is a consequence of the sudden change of boundary condition between the two surrounding mesh points. The numerical approximation and the

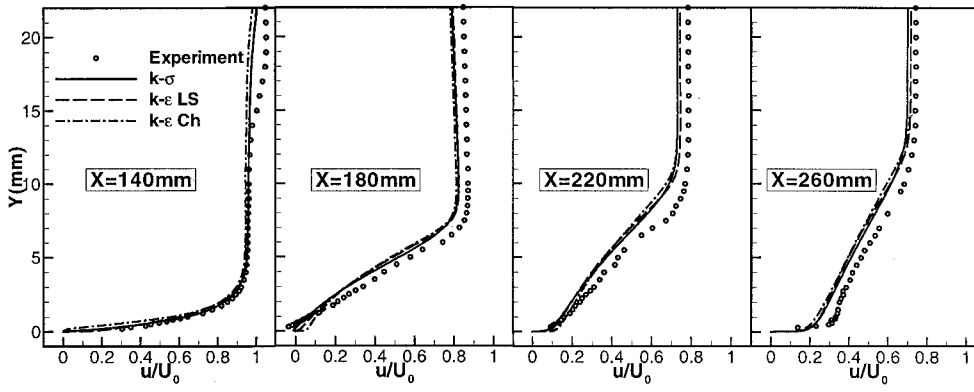

Fig. 8 Longitudinal velocity profiles with passive control.

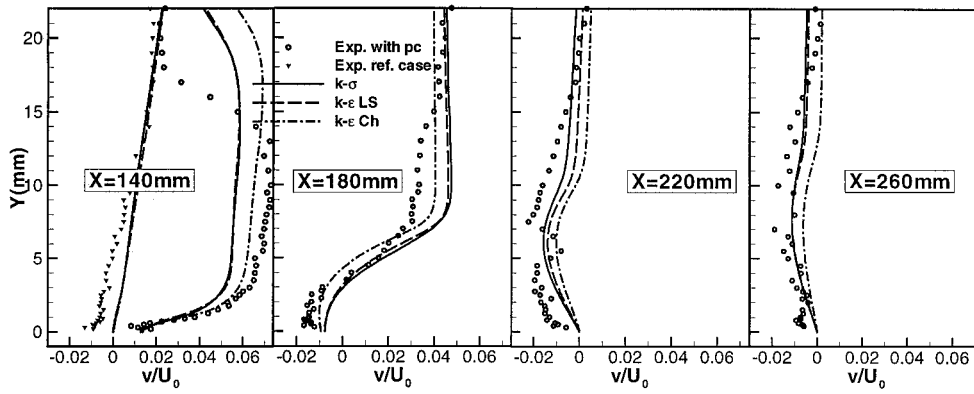

Fig. 9 Transverse velocity profiles with passive control.

experimental resolution are not sufficient to give an account of the true physical process. Downstream of the midcavity, the computed pressure recovers more satisfactory levels. A modification from the imposed experimental pressure levels on downstream boundary was necessary for the k–ε calculations in order to adjust the shock to its experimentally observed position. The amplitude of this shifting can be seen on Fig. 7. The agreement with experiment of computed wall pressure from the end of the cavity to the terminal downstream section is satisfactory with the k–σ model.

Longitudinal velocity levels in the area of maximal wall-pressure gradient (Fig. 8), at the beginning of the cavity ($X = 140$ mm) have been submitted to the effect of the oblique thin compression fan starting from the boundary between the solid and porous walls. The crossing of this compression fan, which affects the experimental longitudinal velocity profiles, can be seen in Fig. 8 between $Y = 15$ and 20 mm. The first mesh point, at which the approximated porous boundary condition is applied, corresponds to the beginning of the porous plate ($X = 130$ mm). For the perforated plate the first row of holes is located at 1.2 mm after the beginning of the plate, which corresponds to the distance between each row of holes. The calculation evaluates a mean normal flux continuously distributed on the plate's surface. This approximation could affect weakly the main features of the global interaction system, like the observed shift between the computed and experimental traces of the compression fan crossing the external part of the velocity profiles. The evolution of the longitudinal boundary-layer velocities in this area of interaction is predicted satisfactorily by the models. An effect of passive control on the experimentally observed interaction is the occurrence of a separated flow of small size at the level of the λ-shock system, above the perforated plate (see schlieren picture in Fig. 1). No recirculating flow appears in the LS calculation; a little recirculating bubble appears between $X = 151$ and 167 mm with the Ch model. The results of the k–σ calculation show a bubble between $X = 145$ and 194 mm. This last recirculating zone extends vertically up to $Y = 0.03$ mm and coincides partly with an area located between $X = 170$ and 200 mm, where small negative values of the longitudinal velocity have been measured at $Y = 0.04$ mm. In any case the calculated reverse longitudinal velocities are located too close to the wall to be compared to experimental values; more measurement points should be needed to correctly define the reversed flow region and thus to validate turbulence models in this separated region. As a consequence of this defective capture of the reversed flow, the response of the boundary-layer flow to local compressions is too roughly simulated by the models. This fact can be observed in Fig. 8 at $X = 180$ and 220 mm. At the end of the interaction area ($X = 220$ mm) and in the downstream boundary layer ($X = 260$ mm), it can be noticed that the velocity defects are more important when passive control is applied. This result is the contrary of the expected boundary-layer bleeding-off effect, which aimed at getting fuller velocity profiles in air intakes.

An important test for the validity of injection modeling at the wall is the prediction of near-wall vertical velocity profiles. As a preliminary verification, the calculated residual mass flow rate per unit span across the perforated plate, which must approach the null experimental value, has been expressed as a ratio of the mass flow rate deficit $\rho_0 U_0 \delta_0^*$ in the upstream boundary layer. In all of the cases, the value of this ratio has been found to be lower than 10^{-5}. More detailed information is presented in Fig. 9. Upstream of the compression system ($X = 140$ mm), wall injection is predicted by all of the models. Data at this station are compared with those obtained without control; these last data make apparent the error bar on the vertical velocity profiles. We verify indeed that these near-wall values without injection, which must clearly tend to zero, are affected of the 1% of U_0 error defined before. When injection is performed, the main global effect is the occurrence of a strong vertical gradient of normal velocity. This induces a supplementary decrease of the longitudinal momentum distribution just before interaction with the shock. In the external part of the boundary layer, global discrepancies of the nonviscous flow have a more spectacular effect on these small velocities; in particular, the location of the calculated crossing expansion fan is about 5 mm higher than the experimental one. Downstream of compression ($X = 180$ mm), a wall suction is found

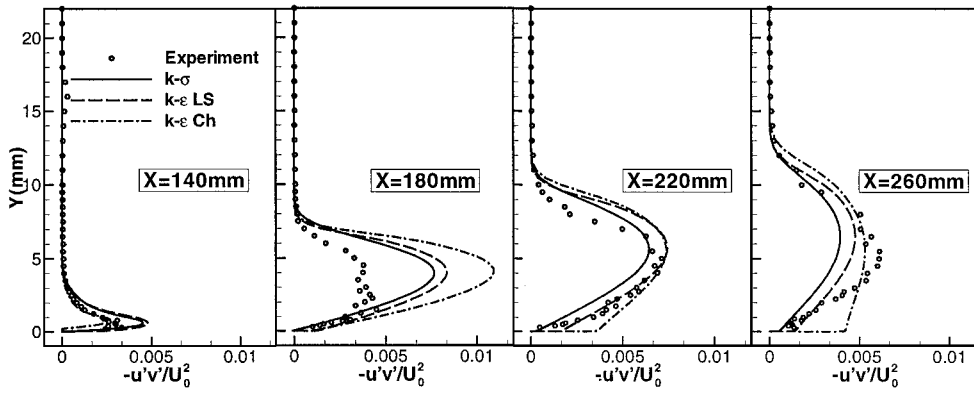

Fig. 10 Turbulent shear-stress profiles with passive control.

by all of the models, as imposed by physics and confirmed by experiment. The effect of the upstream injection is stronger than that of the boundary-layer bleeding-off applied locally in the suction area, and the global result is a thickened downstream boundary layer. To attempt to obtain more satisfactory outgoing velocity profiles, holes situated upstream of the normal shock should be inclined in the downstream direction.[4] As for the upstream injection, the three models predict close values for the small velocity flow sucked at the wall (Fig. 9). Taking into account the experimental uncertainties, this modeling of the passive control of an interaction gives a prediction of the gross tendencies of the field's evolution. The observation of the following predicted profiles downstream of the interaction area confirms the preceding comment.

At the interaction beginning ($X = 140$ mm) the LS and k–σ models anticipate the growth of the maximum $\overline{u'v'}$ level, which is not the case with the Ch model (Fig. 10). The agreement between the LS and k–σ models at $X = 180$ mm is better for this controlled interaction; the Ch model strongly overpredicts the maximum level of $\overline{u'v'}$. Downstream of the interaction area, the better agreement between the LS and k–σ models is confirmed. The main reason for this is that the interaction starting point is fixed precisely at the beginning of the porous wall. In the preceding totally free interaction models found slightly different positions of interaction beginning, which induced an important part of the observed shift in the spatial position between the respective computed interaction domains. The problem of the too rapid near-wall variation of the cross-correlation level in the downstream boundary layer remains with the Ch model.

Conclusions

An exhaustive set of experimental data on free and controlled transonic channel flow interactions has been established with the aim of testing both wall-injection and turbulence models used to simulate such physical situations. A first result is the ability of Poll's injection law, which was established mainly with theoretical arguments, to correctly evaluate the normal velocities at the porous wall when the cavity pressure is known experimentally. Such an efficient evaluation of mass injection should be useful for shortening Navier–Stokes computations aimed to predict the effect of passive control device.

The second result is that the dependency of the models' near-wall behavior with respect to the occurrence of injection has not been evidenced. The necessity of particular modifications of low Reynolds corrections added to a given model for taking into account small velocity injection does not appear clearly at this level of modeling.

The newly defined k–σ model, which was already validated in the case of supersonic backward-facing step separation,[9] has been tested on the present physical situation without modification. This test has been performed by comparison with Chien and Launder–Sharma versions of the k–ε models, which are known to be well calibrated for predicting boundary-layer flows when the grid is sufficiently refined. In comparison with the others, k–σ model uses only a single low turbulent Reynolds number correction, which is done by means of a damping factor of the eddy viscosity. The models appear to represent adequately the gross features of the flow, namely the longitudinal velocity component for all of the models and the wall-pressure levels for the k–σ. If we take into account the experimental uncertainties, the prediction of suction/injection velocities by the models is rather satisfactory. The prediction of the Reynolds stresses, like in any interacting boundary layer, has still to be improved.

Acknowledgment

The present research was accomplished with the financial support of the European Union through the framework of the EUROSHOCK I and II projects.

References

[1] Savu, G., Trifu, O., and Dumitrescu, L. Z., "Suppression of Shocks on Transonic Airfoils," *Proceedings of the 14th International Symposium on Shock Tubes and Shock Waves*, Sydney, Australia, 1983.

[2] Nagamatsu, H. T., Trilling, T. W., and Bossard, J. A., "Passive Drag Reduction on a Complete NACA 0012 Airfoil at Transonic Mach Numbers," AIAA Paper 87-1263, June 1987.

[3] Stanewsky, E., Délery, J., Fulker, J., and Geissler, W., "Euroshock—Drag Reduction by Passive Shock Control," *Notes on Numerical Fluid Mechanics*, Vol. 56, Vieweg, Brunswick, Germany, 1997.

[4] Gefroh, D. L., Hafenrichter, E. S., Ford, B. M., Dutton, J. C., Mc Ilwain, S. T., and Loth, E., "Experimental Study of Mesoflaps for SBLI Control," AIAA Paper 2000-0355, Jan. 2000.

[5] Watterson, J. K., and Raghunathan, S., "Computational Study of Passive Boundary Layer Control Applied to a Supersonic Intake," AIAA Paper 98-0951, Jan. 1998.

[6] Bur, R., Corbel, B., and Délery, J., "Study of Passive Control in a Transonic Shock-Wave/Boundary-Layer Interaction," *AIAA Journal*, Vol. 36, No. 3, 1998, pp. 394–400.

[7] Bur, R., and Corbel, B., "Experimental Study of Transonic Interaction with Shock and Boundary-Layer Control," AIAA Paper 2000-2610, June 2000.

[8] Benay, R., and Servel, P., "Applications d'un Code Navier–Stokes au Calcul d'Écoulements d'Arrière-Corps de Missiles ou d'Avions," *La Recherche Aérospatiale*, No. 6, 1995, pp. 405–426.

[9] Benay, R., and Servel, P., "Two-Equation k–σ Turbulence Model: Application to a Supersonic Base Flow," *AIAA Journal*, Vol. 39, No. 3, 2001, pp. 407–416.

[10] Wilcox, D. C., *Turbulence Modeling for CFD*, DCW Industries, Inc., La Cañada, CA, 1993, Chap. 4.

[11] Speziale, C. G., and Thangam, S., "Analysis of an RNG Based Turbulence Model for Separated Flows," Inst. for Computer Applications in Science and Engineering, Rept. 92-3, Hampton, VA, Jan. 1992.

[12] Chien, K. Y., "Prediction of Channel and Boundary-Layer Flows with a Low-Reynolds-Number Turbulence Model," *AIAA Journal*, Vol. 20, No. 1, 1982, pp. 33–38.

[13] Launder, B. E., and Sharma, B. I., "Application of the Energy Dissipation Model of Turbulence to the Calculation of Flows Near a Spinning Disk," *Letters on Heat and Mass Tranfer*, Vol. 1, No. 2, 1974, pp. 131–138.

[14] Augenstein, E., Bacher, E., Demeautis, C., and Leopold, F., "Influence de l'État de Surface sur l'Écoulement de Culot en Supersonique. Mesures par LDA 2D," 6ème Congrès Francophone de Vélocimétrie Laser, Institut Franco–Allemand de Recherches de Saint-Louis, Saint-Louis, France, Sept. 1998.

[15] Yakhot, V., and Orszag, S. A., "Renormalisation Group Analysis of Turbulence. I. Basic Theory," *Journal of Scientific Computing*, Vol. 1, No. 1, 1986, pp. 3–51.

[16] Bur, R., "Fundamental Study on Passive Control of Shock-Wave/Turbulent Boundary-Layer Interaction in Transonic Flow," Ph.D. Dissertation, Dept. of Mechanics, Univ. of Paris VI, Paris, March 1991.

[17] Warming, R. F., and Beam, R. M., "On the Construction and Application of Implicit Factored Schemes for Conservation Laws," *SIAM-AMS Proceedings*, Vol. 11, Society for Industrial and Applied Mathematics, Philadelphia, 1978, pp. 85–129.

[18] Osher, S., and Chakravarthy, S., "Very High Order Accurate TVD Schemes," Inst. for Computer Applications in Science and Engineering, Rept. 84-44, Hampton, VA, Sept. 1984.

[19] Chanetz, B., Benay, R., Bousquet, J. M., Bur, R., Pot, T., Grasso, F., and Moss, J., "Experimental and Numerical Study of the Laminar Separation in Hypersonic Flow," *Aerospace Science and Technology*, Vol. 2, No. 3, 1998, pp. 205–218.

[20] Yee, H. C., Beam, R. M., and Warming, R. F., "Boundary Approximations for Implicit Schemes for One-Dimensional Inviscid Equations of Gas Dynamics," *AIAA Journal*, Vol. 20, No. 9, 1982, pp. 1203–1211.

[21] Poll, D. I. A., Danks, M., and Humphreys, B. E., "The Aerodynamic Performance of Laser Drilled Sheets," *Proceedings of the First European Forum on Laminar Flow Technology*, Hamburg, Germany, 1992, pp. 274–277.

[22] Maise, G., and McDonald, H., "Mixing Length and Kinematic Eddy Viscosity in a Compressible Boundary Layer," *AIAA Journal*, Vol. 6, No. 1, 1968, pp. 73–80.

R. M. C. So
Associate Editor